Migration of magnetic microparticles through a liquid–liquid interface under an external magnetic field

Sourav Mondal[a], Niki Abbasi[b], Scott S.H. Tsai[b,c,d], Ian M. Griffiths†[e]

[a]*Department of Chemical Engineering, Indian Institute of Technology Kharagpur, Kharagpur 721302, India*
[b]*Department of Mechanical, Industrial, and Mechatronics Engineering, Toronto Metropolitan University, Toronto M5B 2K3, Canada*
[c]*Keenan Research Centre for Biomedical Science, Unity Health Toronto, Toronto M5G 2C4, Canada*
[d]*Institute for Biomedical Engineering, Science and Technology (iBEST) – a partnership between Toronto Metropolitan University and Unity Health Toronto, Toronto M5B 1T8, Canada*
[e]*Mathematical Institute, University of Oxford, Oxford OX2 6GG, United Kingdom*

Abstract

Liquid–liquid interfaces play a pivotal role in various microfluidic processes involving microparticles, including coating, dissolution, controlled release of polyelectrolytes or drugs, and self-assembly processes. In all of these cases, non-invasive techniques to manipulate the microparticle transport are essential. Magnetic manipulation offers an accessible and straightforward means of controlling the motion of magnetic particles within microfluidic devices. Magnetic microparticles are commonly used for conformal polyelectrolyte coating and drug encapsulation by passing them through a liquid–liquid interface, due to their high saturation magnetization, stability, and low toxicity. In this work, we draw inspiration from the lack of studies on the behaviour of magnetic particles near a liquid–liquid interface under conditions of low Reynolds numbers and high capillary action, despite its engineering relevance in microfluidic systems. We consider a canonical flow configuration in which particle motion is driven by the stagnation-point flow that is generated when two different liquids flow towards one another. We show how the operating conditions dictate whether the particle will pierce the interface and become coated or not and illustrate this via parameter-space plots. We use the results of this analysis to understand how the operating conditions influence the fraction of particles that pass through the liquid–liquid interface and are conformally coated, which may be used to guide a variety of industrial processes.

Keywords

†Address for correspondence: ian.griffiths@maths.ox.ac.uk

Microfluidics; magnetic field; particle migration; liquid-liquid interface; coating

1. Introduction

Liquid–liquid interfaces in microfluidic devices have attracted considerable attention as a result of their importance in encapsulation and coating. Inertial effects and hydrodynamic drag drive particles through a liquid–liquid interface, allowing them to be conformally coated in one of the two liquid phases. Magnetic material may be added to the particles to provide a non-invasive method to control and direct particle movement, providing precise manipulation capabilities at the micro and nano scales.

Specific examples at the laboratory scale include the self-assembly and conformal coating of magnetic microparticles using a two-phase co-flow oil–water interface and a magnetic field [1]; drug encapsulation of a ferrofluid droplet using a magnetic field [2, 3]; multi-layer magnetic polyelectrolyte encapsulation using droplet microfluidics [4]; and targeted cell sorting and separation technology using magnetic nanoparticle labels [5].

Such processes may be applied in a broad range of practical scenarios. Targeted drug delivery across biological barriers, such as the blood–brain barrier or cellular membranes can enhance efficacy and reduce the side effects of therapeutic treatments [6, 7, 8, 9]. In magnetic hyperthermia techniques used in cancer treatment, magnetic nanoparticles are used to heat and destroy cancer cells, all involving precise and controlled transport across liquid interfaces [10]. Furthermore, understanding the transport of magnetic particles through liquid–liquid interfaces in the renal system can ensure precise targeting in the treatment of kidney stones, potentially allowing for non-invasive or minimally invasive treatments [11].

A considerable body of literature exists on studies of the motion of magnetic particles in liquids under an external magnetic field and their behaviour near interfaces in the limiting cases where either (a) the inertial forces are much greater than the capillary forces, and the particles pass through the interface unperturbed, or (b) the inertial forces are much weaker than the capillary forces, and the interface is unperturbed by the particle, which sees the interface as effectively rigid. However, the response when these forces are in balance, as is often the case in the aforementioned physical examples, has been much less explored. As a result, the method of optimizing such set-ups for a given outcome is not well known.

There have been several literature studies on the dynamics of a particle near a liquid–liquid interface [12] or how a particle deforms the interface in the process of transportation [13]. However, these studies do not address the impact of the magnetic field on the motion of the particle. The transport of microspheres under the action of magnetic field was first reported by Driscoll et al. [14], which was extended by Grief et al. [15] taking into account the interactions with moving red blood cells in the fluid and analysing the behaviour in a branched fluid flow network. The work by Grief et al. [15] was focused on designing an appropriate magnetic field to manipulate the magnetic particles in the desired direction. In another review by Friedman and Yellen [16], the effect of the magnetic field relative to the gravitational and electrical forces on magnetic particle separation and sorting was discussed. However, the role of the liquid interface in the trajectories of the magnetic particles was not considered. Thus, in order to understand the behaviour of particles in the aforementioned physical processes, it is imperative to couple the knowledge of the fluid flow and magnetism with the behaviour at liquid–liquid interfaces.

In this paper, we study the transport of a particle under the combined influence of the viscous and magnetic field in a microfluidic environment. Specifically, we consider the behaviour of magnetic particles under the influence of an external field, when placed in a canonical stagnation-point flow formed by opposing liquid streams.

We begin in Section 2.1 by studying the flow field and the shape of the liquid–liquid interface as the inflow rate is varied. We then introduce a magnetic field in Section 2.2, and describe the resulting equations of motion for the particles in Section 2.3. In Section 2.4 we analyse the influence of inlet location on the capture, interface penetration, or escape of magnetic particles within a microfluidic system. We find that the behaviour is described by three key parameters: the Mason number, which characterizes the ratio of viscous to magnetic forces, the capillary number, which describes the interfacial tension relative to the viscous forces, and the viscosity contrast between the two liquids.

We distil the results into convenient parameter-space plots that allow for easy understanding of the operating regimes that will lead to conformal coating of the particles via interfacial penetration. Finally, in Section 4, we draw conclusions on the application of the work to practical scenarios.

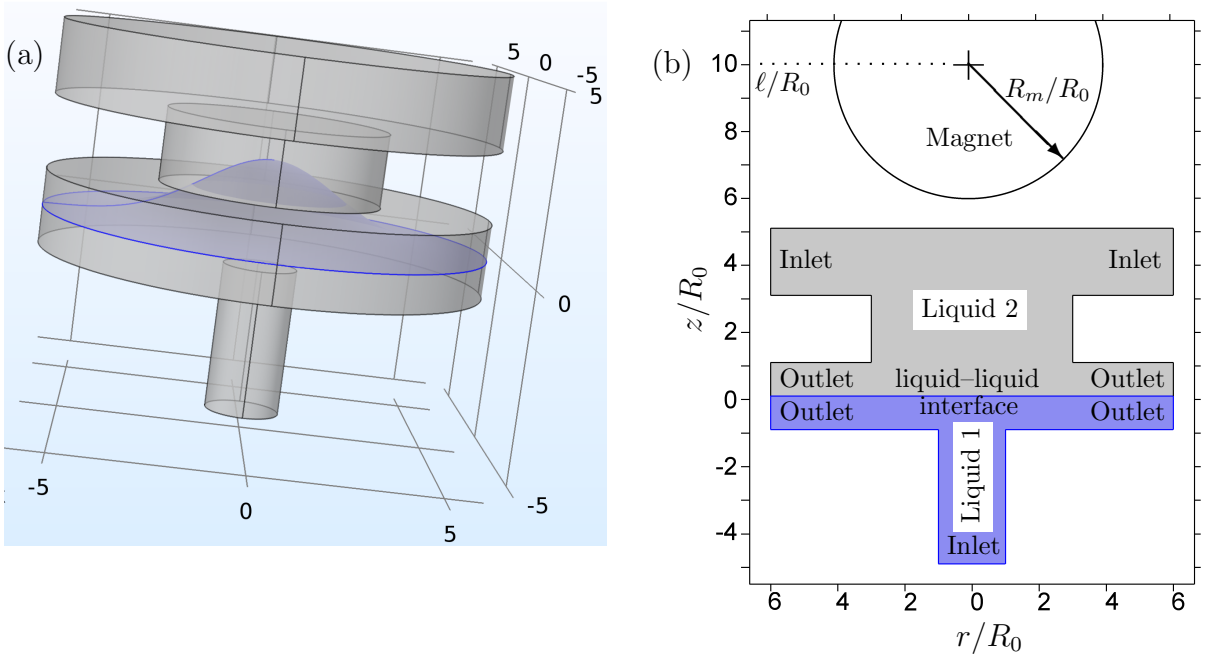

Figure 1: (a) The 3D representation of the set-up illustrating the axisymmetric properties of the device. The blue shaded surface is the 3D rendering of the deformed liquid interface in the presence of a flow. (b) Schematic of the geometrical set-up of the reduced model, in cylindrical polar coordinates, $(r/R_0, z/R_0)$ scaled with the inlet radius, R_0. The liquid–liquid interface is located at $z = 0$ in the absence of a flow (as illustrated in b) but will deform when an inflow is applied (as illustrated in a).

2. Model

We model the set-up as a two-liquid system where the magnetic particles are introduced in one liquid and their trajectories are influenced by both the liquid flow and an external magnetic field. We suppose that the liquids are non-conducting so that they do not respond themselves to the magnetic field. The geometry we consider is depicted in Fig. 1(a), which captures the salient features of a typical microfluidic system geometry we wish to consider. Specifically, we adopt an axisymmetric coordinate system, (r, z), motivated by the symmetry of the system exposed in Fig. 1(b). We focus our attention on the device behaviour when operating in its steady-state flow configuration. We define the liquid–liquid interface as $z = h(r)$ and set the z axis to lie on the line that separates the two liquids in the absence of any inflow and outflow (so that $h(r) = 0$ in the absence of any flow).

2.1. Liquid flow and interfacial profile

We denote the liquid velocities $\boldsymbol{u}_i = u\hat{\boldsymbol{r}} + w\hat{\boldsymbol{z}}$, for $i = 1, 2$ with $\hat{\boldsymbol{r}}$ and $\hat{\boldsymbol{z}}$ representing unit vectors in the r and z direction respectively, and the liquid pressures, densities and viscosities by p_i, ρ_i and μ_i, respectively, for $i = 1, 2$. We consider a dimensionless system,

generated via the following scalings:

$$R = \frac{r}{R_0}, \qquad Z = \frac{z}{R_0}, \qquad U_i = \frac{u_i}{u_0}, \qquad W_i = \frac{w_i}{u_0}, \qquad P_i = \frac{pR_0}{\mu_2 u_0}, \qquad H = \frac{h}{R_0}. \tag{1}$$

Here R_0 is the inlet radius of the system and u_0 is the inlet velocity, which we assume to be plug flow (defined in Table 1). The system is described by the dimensionless steady axisymmetric incompressible Navier–Stokes equations,

$$\nabla \cdot \boldsymbol{U}_i = 0, \tag{2a}$$

$$\mathrm{Re}_i\big(\boldsymbol{U}_i \cdot \nabla \boldsymbol{U}_i\big) = -\nabla P_i + \alpha_i \nabla^2 \boldsymbol{U}_i \tag{2b}$$

where $\mathrm{Re}_i = \rho_i u_0 R_0/\mu_2$, and $\alpha_i = \mu_i/\mu_2$, denote respectively the Reynolds number in each liquid and the viscosity contrast (see Table 1 for the values taken for these simulations).

Table 1: Parameter definitions and values

Parameter, symbol [units]	Typical values
Magnetization constant, M [A/mm]	1.05×10^4
Magnetic permittivity of vacuum, μ_0 [J/A^{2}m]	1.26×10^{-7}
Magnetic susceptibility, χ_e	0.01
Liquid viscosity, μ_2 [Pa s]	0.01
Liquid density, ρ_i $(i = 1, 2)$ [kg m^{-3}]	1000
Inlet radius, R_0 [mm]	0.125
Inlet velocity, u_0 [m/s]	0.004
Radius of the magnet, R_m [mm]	0.5
Interfacial tension, γ [mN/m]	0.04
Distance of the magnet centre from origin, ℓ [mm]	10

Parameter, symbol	Definition	Typical values
Reynolds number, Re_i	$\dfrac{\rho_i u_0 R_0}{\mu_2}$	0.06
Mason number, Mn_i	$\dfrac{\mu_i u_0 R_0}{\mu_0 \chi_e a^2 M^2}$	0.0033
Viscosity contrast, α_i	$\dfrac{\mu_1}{\mu_2}$	1–10
Inverse capillary number, Γ	$\dfrac{\gamma}{\mu_2 u_0}$	1
Dimensionless magnet distance, L	$\dfrac{\ell}{R_0}$	80

Eqs. (2) are solved subject to the following boundary conditions (refer to Fig. 1a for

schematic illustrating boundaries):

$$W_1 = 1, \quad U_1 = 0 \qquad \text{at liquid inlet 1,} \tag{3a}$$

$$U_2 = -0.25, \quad W_2 = 0 \qquad \text{at liquid inlet 2,} \tag{3b}$$

$$\text{zero total stress, } \boldsymbol{T}_i = -P_i \boldsymbol{I} + \alpha_i \nabla \boldsymbol{U}_i = 0, \qquad \text{at the outlets,} \tag{3c}$$

$$\text{Axisymmetry, } U = 0, \quad \frac{\partial W}{\partial R} = 0 \qquad \text{at } R = 0, \tag{3d}$$

$$\text{No slip and no penetration, } \boldsymbol{U}_i = 0, \qquad \text{on remaining geometry walls,} \tag{3e}$$

where $\boldsymbol{I}$ denotes the identity matrix. At the liquid–liquid interface, the velocity field and the stresses are continuous

$$\boldsymbol{U}_1 \cdot \boldsymbol{t} = \boldsymbol{U}_2 \cdot \boldsymbol{t} \equiv U_{\text{int}}, \tag{3f}$$

$$\boldsymbol{n} \cdot [\boldsymbol{T}_1 - \boldsymbol{T}_2] = \Gamma \left(\nabla \cdot \boldsymbol{n}\right) \boldsymbol{n}, \tag{3g}$$

where $\boldsymbol{n}$ is the unit outward-pointing normal to Liquid 1, $\boldsymbol{t}$ is the unit tangent to the interface and U_{int} is the interfacial (tangential) liquid velocity. Here $\Gamma = \gamma/\mu_2 u_0$ is the inverse capillary number, which provides a measure of the interfacial tension, with γ the surface tension between the two liquids.

The set of partial differential equations (2) are solved numerically subject to the boundary conditions (3), using the finite-element package COMSOL® v5.3 to obtain the flow and pressure fields (U_i, W_i) and P_i, for $i = 1, 2$, and the equilibrium interface. We show the interfacial profile for different viscosity ratios (α_1) and interfacial tensions (Γ) in Fig. 2(a) and the flow streamlines for an example case in Fig. 2(b).

2.2. Magnetic force field

We now introduce a magnetic field, generated by a spherical permanent magnet of radius R_m. In dimensional form, this is expressed in cylindrical polar coordinates as [17]:

$$\boldsymbol{\mathcal{H}} = \frac{M R_m^3}{\left[(z-\ell)^2 + r^2\right]^{5/2}} \left\{ (\ell - z) r \hat{\boldsymbol{r}} + \frac{1}{3}\left[(z-\ell)^2 - r^2\right] \hat{\boldsymbol{z}} \right\}, \tag{4}$$

where M is the magnetization of the magnet and ℓ is the distance (in the z direction) from the axes origin to the magnet centre (see Fig. 1). The dimensional magnetic dipole moment $(\boldsymbol{m})$ experienced by a particle of radius a due to the magnetic field $\boldsymbol{\mathcal{H}}$ is [18]

$$\boldsymbol{m} = \frac{4}{3} \chi_e \pi a^3 \boldsymbol{\mathcal{H}}, \tag{5}$$

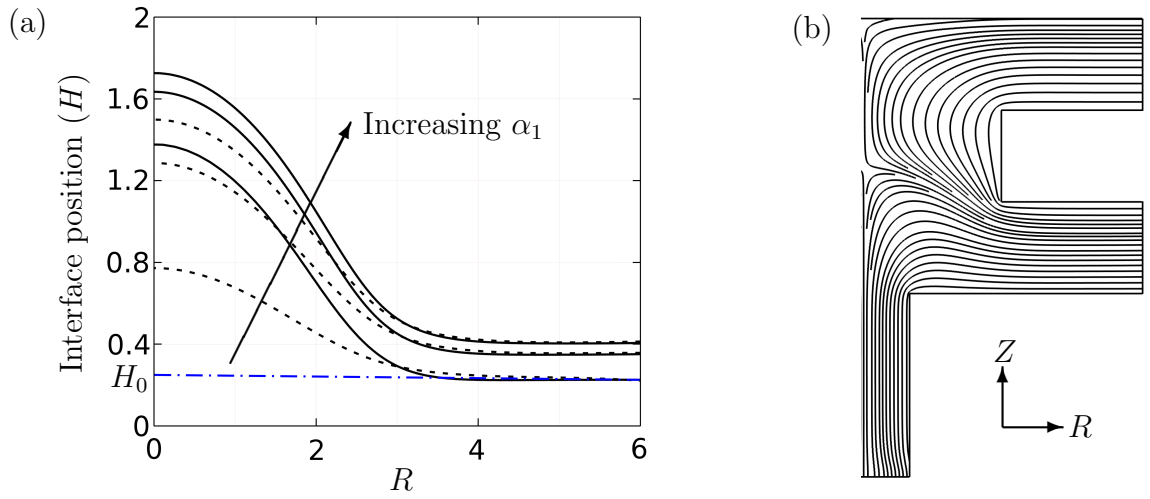

Figure 2: (a) Interface profile as a function of the radial distance, for Re = 0.06. The arrow indicates the interface profile for increasing $\alpha_1 = 1$, 5 and 10. The solid and dotted black curves represent $\Gamma = 0$ and 10, respectively. The dot-dashed (blue) curve $H = H_0$ is for $\Gamma \gg 1$ and $\alpha_1 = 1$, which is shifted from $Z = 0$ as a result of the liquid flow. (b) The flow streamlines in the case of a fully developed (equilibrium) liquid interface with $\alpha_1 = 10$ and $\Gamma = 0$.

where χ_e is the effective magnetic susceptibility of the medium. The dimensional force acting on the particle due to the magnetic field is then [19]

$$\boldsymbol{f} = \frac{\mu_0}{2}\nabla\big[\boldsymbol{m}\cdot\boldsymbol{\mathcal{H}}\big] = \frac{2}{3}\pi\mu_0\chi_e a^3\nabla\boldsymbol{\mathcal{H}}^2, \tag{6}$$

where μ_0 is the permeability of free space. Eq. (6) can be expanded and non-dimensionalized via

$$\boldsymbol{f} = f_r\hat{\boldsymbol{r}} + f_z\hat{\boldsymbol{z}} = \frac{4\pi\mu_0\chi_e a^3M^2}{27R_0}(F_r\hat{\boldsymbol{r}} + F_z\hat{\boldsymbol{z}}) = \frac{4\pi\mu_0\chi_e a^3M^2}{27R_0}\boldsymbol{F}, \tag{7}$$

where

$$F_r = \frac{\left[2(L-Z)^4 - 3R^4 - 26R^2(L-Z)^2\right]R}{\left(R^2+(L-Z)^2\right)^6}, \tag{8}$$

$$F_z = \frac{\left[3(L-Z)^4 - 2R^4 + 26R^2(L-Z)^2\right](L-Z)}{\left(R^2+(L-Z)^2\right)^6}, \tag{9}$$

and $L = \ell/R_0$.

2.3. Particle trajectories

The trajectories of the magnetic particles are obtained by balancing the hydrodynamic drag and the magnetic force experienced by the particle, assuming that inertial effects are negligible:

$$6\pi\mu_i a\left(\boldsymbol{u}_i - \boldsymbol{u}_p\right) + \boldsymbol{f} = 0, \tag{10}$$

for $i = 1, 2$, where $\boldsymbol{u}_p = \mathrm{d}\boldsymbol{r}_p/\mathrm{d}t$ is the particle migration velocity and $\boldsymbol{r}_p = (r_p, z_p)$ denotes the particle location. Upon non-dimensionalization, Eq. (10) becomes

$$\frac{\mathrm{d}\boldsymbol{R}_p}{\mathrm{d}T} = \boldsymbol{U}_i + \frac{2}{81\mathrm{Mn}_i}\boldsymbol{F}, \tag{11}$$

for $i = 1, 2$, where

$$\boldsymbol{R}_p = \frac{\boldsymbol{r}_p}{R_0}, \qquad\qquad T = \frac{u_0 t}{R_0}, \tag{12}$$

and $\mathrm{Mn}_i = (\mu_i u_0 R_0)/(\mu_0 \chi_e a^2 M^2)$ is the Mason number, describing the ratio of the viscous to the magnetic force in each of the two liquids. Equation (11) may be separated into components and rearranged to give the migration velocities,

$$\frac{\mathrm{d}R_p}{\mathrm{d}T} = U_i + \frac{2F_r}{81\mathrm{Mn}_i}, \qquad \text{and} \qquad \frac{\mathrm{d}Z_p}{\mathrm{d}T} = W_i + \frac{2F_z}{81\mathrm{Mn}_i}, \tag{13}$$

for $i = 1, 2$. Eq. (13) can be solved to determine the particle trajectories given the flow field, (U_i, W_i), for $i = 1, 2$ obtained from Section 2.1.

2.4. Particle behaviour

The particle will move in Liquid 1 due to the magnetic force until it reaches the interface. At this point, the particle will locally deform the interface, which will generate a restoring force that resists the transmission of the particle across the interface. Whilst we do not model the local interfacial deformation explicitly here, we assume that when the driving force due to the flow and magnetization exceeds the maximum normal restoring force that can be provided, that is, $f_s = 2\pi\gamma a$, the particle will pass through the interface. This corresponds to a maximum dimensionless restoring force

$$F_s = \frac{27}{2}\mathrm{Mn}_1\Gamma. \tag{14}$$

If the particle does not pass through the interface it will move along this surface. By taking the scalar product of (11) with $\boldsymbol{t}$ we see that the particle will move towards the centre if $\boldsymbol{F}\cdot\boldsymbol{t} > F_v$ and away from the centre if $\boldsymbol{F}\cdot\boldsymbol{t} > F_v$, where

$$F_v = \frac{81}{2}\mathrm{Mn}_1 U_{\mathrm{int}}. \tag{15}$$

The particle motion can thus be categorized into one of four possible scenarios:

Case (i) *No capture or penetration*:

$$\text{If} \qquad \boldsymbol{F}\cdot\boldsymbol{n} < F_s, \qquad \text{and} \qquad \boldsymbol{F}\cdot\boldsymbol{t} < F_v, \tag{16}$$

then the particle will arrive at but not penetrate the interface. Alternatively, the hydrodynamic drag might be so large that the particle never makes it to the interface. In both of these cases, the particle passes through the device outlet in Liquid 1 (Fig. 3a).

Case (ii) *Penetration but not capture*:

$$\text{If} \qquad \boldsymbol{F}\cdot\boldsymbol{n} > F_s, \qquad \text{and} \qquad \boldsymbol{F}\cdot\boldsymbol{t} < F_v, \tag{17}$$

then the particle will penetrate the interface but leave through the device outlet in Liquid 2 (Fig. 3b).

Case (iii) *Relocation towards the centre, subsequent penetration and capture*:

$$\text{If} \qquad \boldsymbol{F}\cdot\boldsymbol{n} < F_s, \qquad \text{and} \qquad \boldsymbol{F}\cdot\boldsymbol{t} > F_v, \tag{18}$$

then the particle migrates along the interface towards $R = 0$. The particle penetrates if $F_z > F_s$ at $z = 0$ (since the hydrodynamic drag is zero here) or remains trapped on the interface at $R = 0$ otherwise. Upon penetration, since the magnetic force is larger than the hydrodynamic drag in Liquid 1, it will be even larger in Liquid 2, and will thus subsequently be captured by the magnet (Fig. 3c).

Case (iv) *Penetration and capture*:

$$\text{If} \qquad \boldsymbol{F}\cdot\boldsymbol{n} > F_s, \qquad \text{and} \qquad \boldsymbol{F}\cdot\boldsymbol{t} > F_v, \tag{19}$$

then the particle will penetrate the interface and be captured (Fig. 3d).

Each of these penetration cases has its unique application merit. Case (i) has an unique application owing to the entrapment of the particles at the interface, where it is exposed to both the liquids. This is useful for synthesizing magnetic Janus particles [20] coating with two different materials, and controlled dynamic wetting behaviour which influence the interfacial rheology and microscopic inter-particle interactions at the interface [21]. Case (ii) corresponds to the conformal coating of the particles, which is relevant to applications such as drug encapsulation. Case (iv) corresponds to the facilitation of mass transfer across the interphase [22], which is relevant in targeted micro- (or nano-)

particle delivery in renal intervention, kidney stone removal, and drug delivery in tissues. Case (iii), in which the particle takes a convoluted trajectory to reach the magnet, is applicable for directed self-assembly, promoting ordered structures, and controlled cluster formation [23].

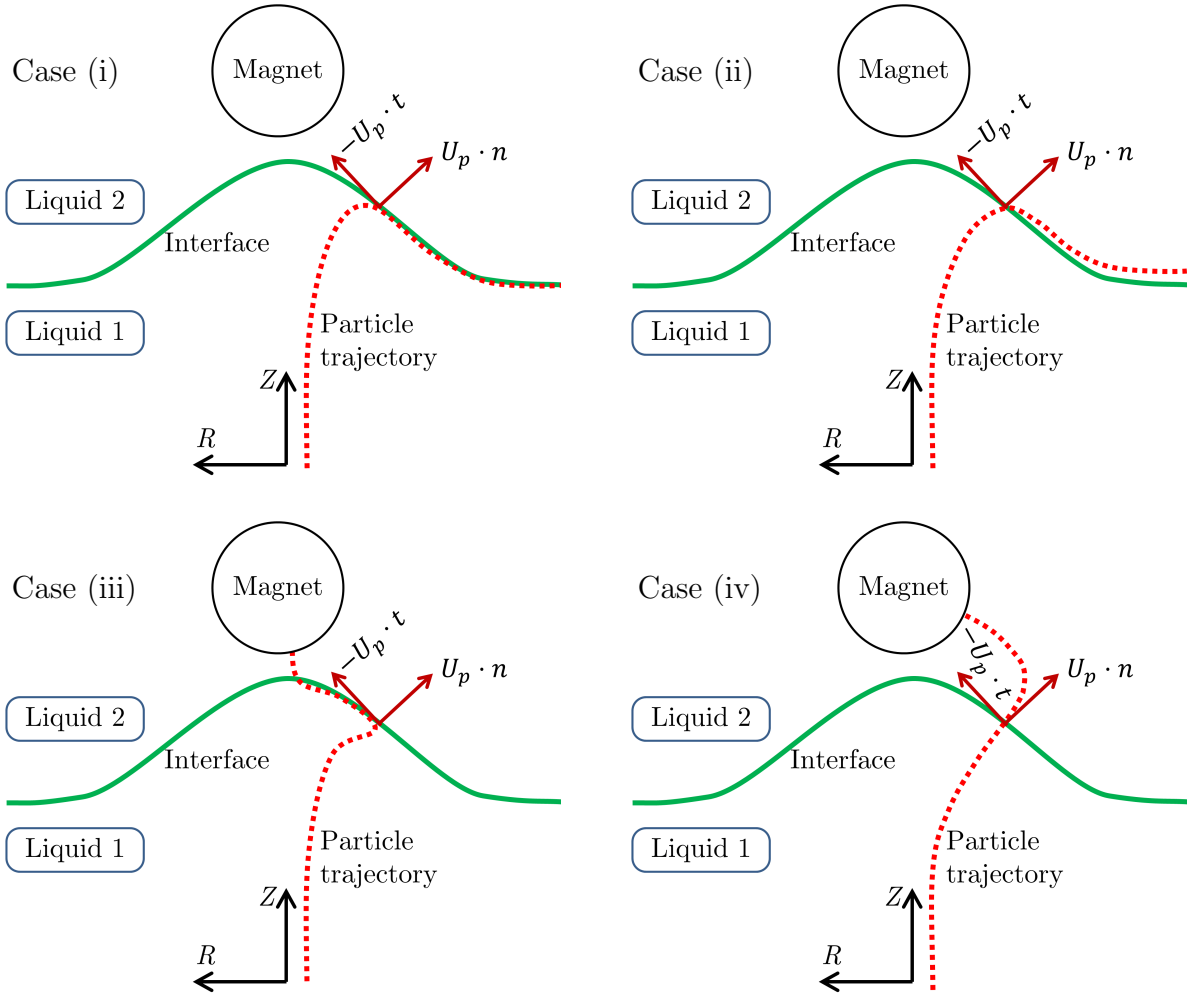

Figure 3: Schematic representation of the four different scenarios in particle migration.

3. Results and Discussion

Particles are introduced into the system in Liquid 1 through the inlet, located at $Z = -5$ and different radial locations, $R = R_{\text{in}} \in [-1, 1]$. The trajectories of the magnetic particles for different inlet radial positions R_{in} and Mason numbers Mn_2 are shown in Fig. 4. The limiting particle position (R^*) is defined as the introductory radial particle position R_{in} such that all particles with introductory positions $R_{\text{in}} < R^*$ are trapped in the device and all particles introduced at $R_{\text{in}} > R^*$ escape the device (Fig. 4a).

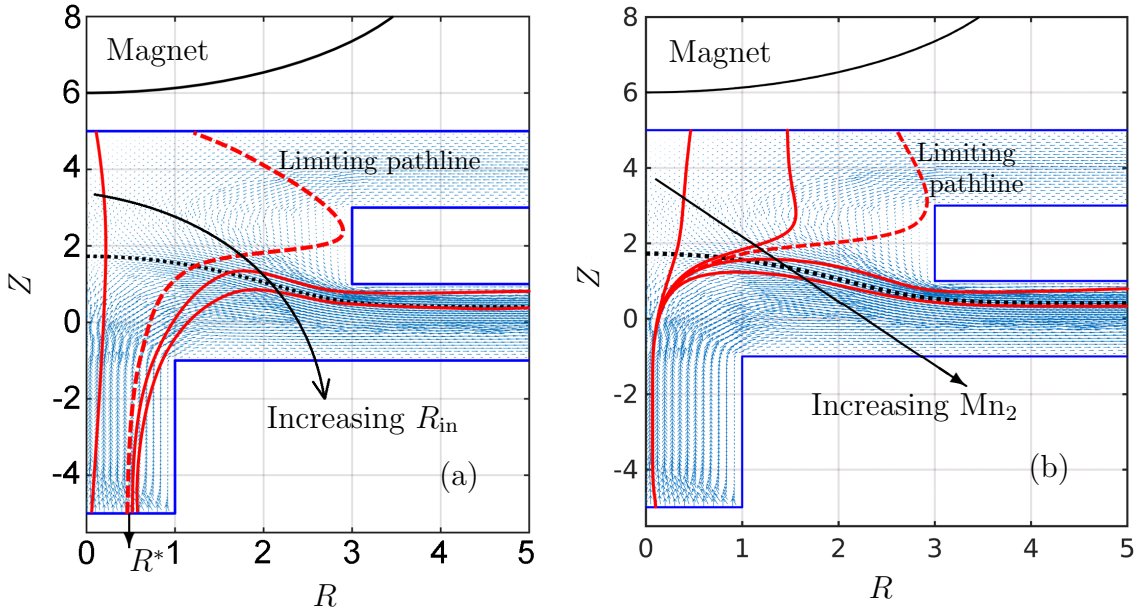

Figure 4: Magnetic particle trajectories (solid red curves) in the liquid for (a) varying inlet location $R_{\text{in}} = 0.04$, 0.52, 0.57 and 0.61 with fixed Mason number $\text{Mn}_2 = 1.75 \times 10^{-4}$, and (b) varying Mason numbers $\text{Mn}_2 = (1, 3.2, 5.3, 6.9, 10) \times 10^{-4}$ with fixed inlet location $R_{\text{in}} = 0.08$. In both cases, $\Gamma = 0$, $\alpha_1 = 10$, and the particles are introduced at $Z = -5$. The blue arrows in the figure represent the liquid streamlines and the black dotted line denotes the liquid–liquid interface. The red dashed line represents the limiting pathline, which separates particles captured by the magnet from those that escape through the outlet. The values of the other parameters are listed in Table 1.

We examine the parameter dependence of R^* in Fig. 5. We observe a non-monotonic relationship of R^* with Mn_2. This arises due to two competing effects. First, for large Mason numbers, increasing the Mason number gives rise to a reduction in R^*. We may identify this with the intuitive result that a reduction in the magnetic field strength leads to a reduction in capture efficiency. However, we also observe that for small Mason numbers, a decrease in Mason number also reduces the value of R^*. This second result emerges because reducing the liquid viscosity leads to less interface deformation, which in turn means that the particles that collect at the interface are further away from the magnetic field, and thus the force experienced is less [24]. Overall, this gives rise to an optimum Mason number that maximizes the number of particles that are trapped.

This physical justification is supported by examining the behaviour for different values of the viscosity contrast (comparing Figs. 5a and b). Similarly, for low values of the Mason number, the higher viscosity contrast gives rise to higher values of R^*, due to the reduction in interface deformation, while for higher values of the Mason number, it is the lower viscosity contrast that yields higher values of R^*.

The dependence of the behaviour of R^* on inverse capillary number, Γ, is similarly

explained. Specifically, for large Mason numbers, increasing Γ reduces the value of R^*, since the force required to penetrate the interface rises with increasing Γ, and so the ability to be captured by the magnet reduces. However, for small Mason numbers, increasing Γ increases the value of R^*, as a result of the reduction in interface deformation that means particles at the interface are further from the magnet.

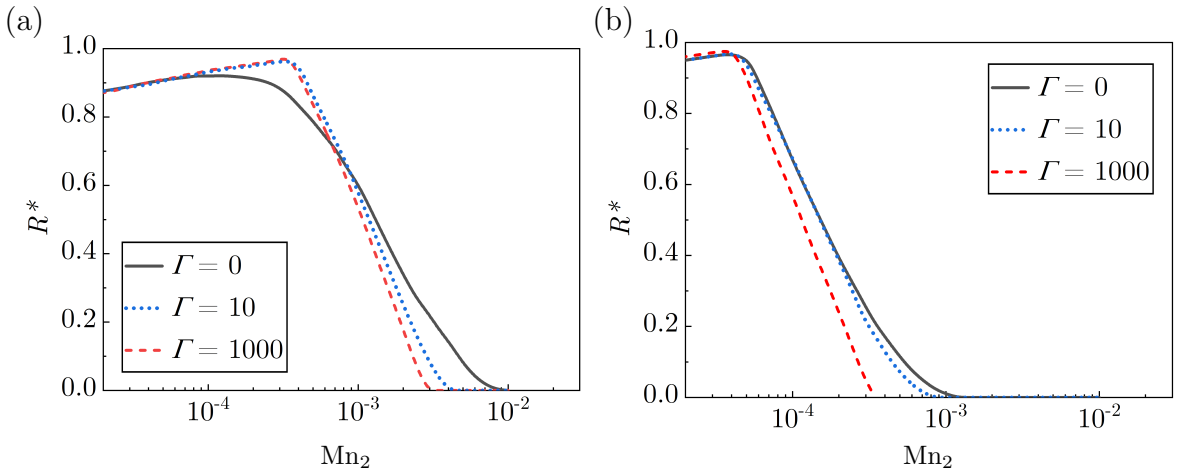

Figure 5: The limiting position R^* below which injected particles are captured, as a function of the Mason number for (a) $\alpha_1 = 1$ and (b) $\alpha_1 = 10$.

In Fig. 6 we build upon the observations made in Fig. 5 by illustrating the role of the parameter choice on selecting the system behaviour, as outlined in the four cases in Fig. 3, via a phase-space diagram. The curve that separates Case (i) corresponds to the separating curves, $R^*(\mathrm{Mn}_2)$, in Fig. 5.

When the value of Γ is large, the interface is nearly flat, irrespective of the fluid viscosity contrast α_1. This results in the disappearance of Case (iii), since this is possible only in the presence of a deformed interface (Fig. 3c,d). For nearly flat interfaces, the balance between the viscous drag and magnetic force parallel to the interface becomes very sensitive, which gives rise to non-intuitive behaviour. In the case of a flat interface and high viscosity contrast we observe a wide range of the parameter space for which the particles penetrate the interface but escape the system without capture (Fig. 3d). This arises because as the particle moves into Fluid 2, in which the viscosity is lower, the interface velocity is higher, which enhances the particle's motion towards the exit. Overall, Fig. 3 demonstrates how one can control particle behaviour by manipulating the particle inlet location and the magnetic field [25].

Finally, we make the observation that non-capture by the magnetic does not neces-

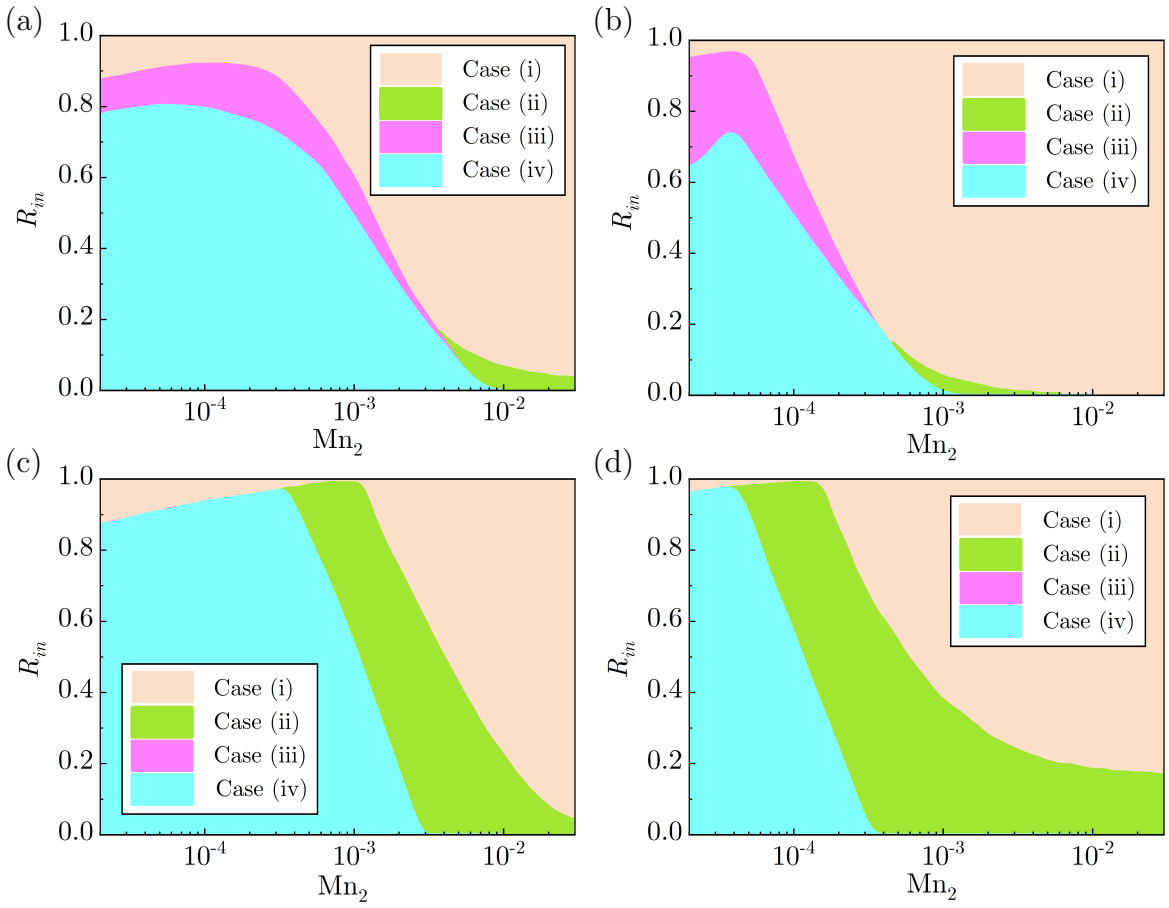

Figure 6: Phase space diagram of the different possible cases as explained in Fig. 3, for various parameter values. The scenarios in (a) $\alpha_1 = 1$ and (b) $\alpha_1 = 10$ are for $\Gamma = 0$, while (c) $\alpha_1 = 1$ and (d) $\alpha_1 = 10$ are for the nearly flat interface, $\Gamma = 1000$. The distinction between the criteria of capture and no-capture scenarios is delineated between Case (ii) and (iii). In sub-figures (c) and (d), the phase space zone for Cases (iii) and (iv) are overlapping.

sarily imply that the particles escape in an $O(1)$ amount of time. Specifically, in each of these cases, we find that some particles may end up residing very close to the walls of the device, where the fluid velocity is extremely low and so the particles become effectively stuck. While we emphasize that the particles have no mechanism of adhesion to the wall, those that do become close enough can take up to 10^3 times longer to escape the device. Such cases are designated as *resting* at the walls. We thus subcategorize Cases (i) and (ii) further, into the following scenarios:

Case (i)A. *Particle retarded by inlet wall.*

Case (i)B. *Particle retarded by lower domain wall.*

Case (i)C. *Particle remains in interface 1 but escapes in finite time.*

Case (ii)A. *Particle penetrates interface escapes in finite time.*

Case (ii)B. *Particle retarded by upper domain wall.*

Each of these subcategories is illustrated in Fig. 7. Each of these subcategories has its own features, leading to operational constraints and undesirable circumstances. For instance, the accumulation of particles on the inlet walls in Case (i)A can result in flow constriction.

In Fig. 7, we illustrate the various possibilities that may arise in the system. For higher viscosity contrasts, the viscous drag pulling the particles towards the exits is higher, and so the particles are less likely to find themselves in a resting state. This is seen by the shrinkage of the region of Case (i)B as we move from Fig. 8(a) to (b), and from Fig. 8(c) to (d).

We observe that Case (ii)A does not arise in the case of a nearly flat interface (Fig. 8c,d) [26]. As the interfacial tension is high, the particle needs a large magnetic force to cross over into Liquid 2. Hence, once in Liquid 2, the particle will always be attracted to the magnet.

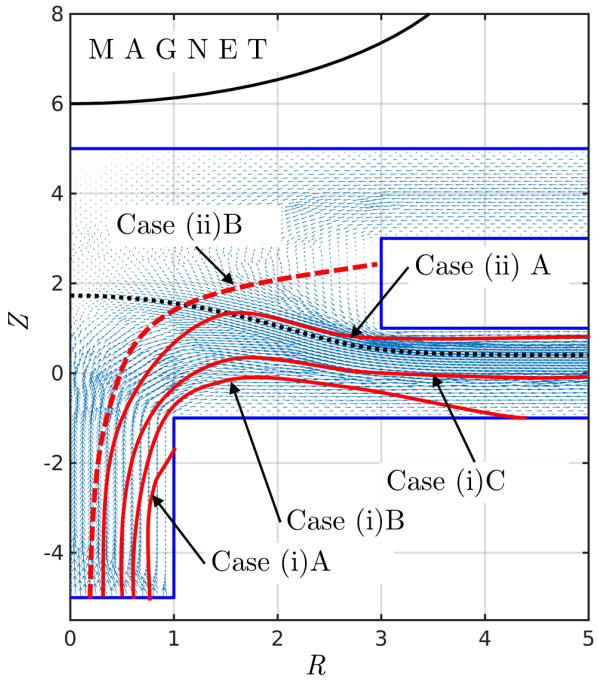

Figure 7: Schematic representation of the different subcategories of Cases (i) and (ii).

4. Conclusions

The understanding of how magnetic particles interact with and traverse liquid–liquid interfaces plays an important role in the development of new methods for the controlled

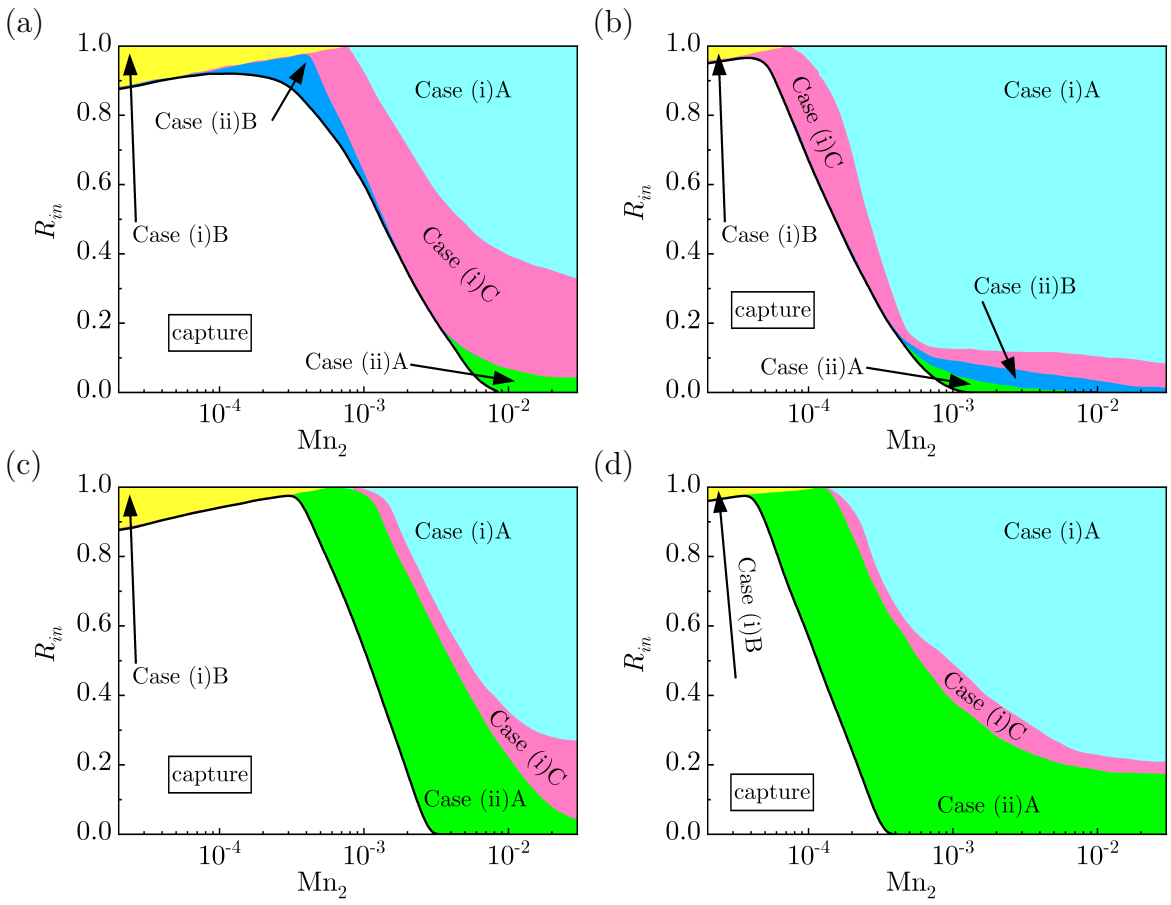

Figure 8: Phase-space diagram of the different possible sub-classifications of the no-capture scenarios, as explained in Fig. 7, for various parameter range. The sub-figures (a) $\alpha_1 = 1$ and (b) $\alpha_1 = 10$ are for the deformed interface ($\Gamma = 0$), where as (c) $\alpha_1 = 1$ and (d) $\alpha_1 = 10$, are for the undeformed case $\Gamma = 1000(\equiv \infty)$.

transport of substances across these boundaries. This process arises in applications including drug encapsulation, coating processes, and controlled release, where precise particle transport control at liquid–liquid interfaces is critical.

The results of our work reveal the interplay between the process conditions that determine when a microparticle can successfully migrate through the liquid–liquid interface. For a uniform particle distribution across the inlet, our results tells us the fraction of particles that will be captured. After crossing through the interface, the particle can take different routes, either migrating parallel to the interface or moving towards the magnet. These results can determine the operating regimes to achieve multi-layer conformal coating or encapsulation in multi-laminar flow process [1]. We also demonstrated how particles that are not trapped by the magnet can either exit through the outlets in an order-one timescale, or become 'trapped' close to the walls of the chamber, where the velocities are low, and thus taking orders of magnitude longer before they eventually

exit from the device. This provided further categorization of the potential behaviour of particles within our device.

Deflection or directed flow of magnetic microparticles [27] or magnetic droplets [28] across multi-laminar flow streams is a key component of rapid and automated fabrication of polymer-multilayer-capsules [3]. The system we study here possesses many of the features that are important in achieving the desired level of polyelectrolyte coating thickness (manipulating the path of the particle migration and thus the residence time), multi-layer coating (by alternating magnetic field directions), targeted cell sorting, and separation technology (using magnetic nanoparticle labels).

There are various natural open areas that warrant further development. First, in the case of high concentration of magnetic particles, there will be particle aggregation and the drag on the particle clusters must be modelled appropriately. Second, generally the magnetic particles (or ferrofluid droplets) are polydisperse in nature, and so it would be natural to study a distribution of different particle sizes in our model. Finally, there is significant interest in the behaviour of active particles at liquid–liquid interfaces [29]. Generalizing our work to allow for such active motion would provide valuable insights into this area to understand how one can promote or inhibit their motion.

Insights from this research can aid in designing and synthesizing novel materials with unique properties, such as responsive or self-healing materials, bottom-up assembly of nanoparticles into structured arrays or functional coatings, and exploiting interfaces as scaffolds for ordered structures.

Acknowledgements

SM gratefully acknowledges the support from the Royal Society and EPSRC for funding. SM also acknowledges the travel grant and subsistence support from the Mathematical Institute (University of Oxford) and the CPDA funding (IIT Kharagpur).

References

[1] Alorabi, A.Q., Tarn, M.D., Gómez-Pastora, J., Bringas, E., Ortiz, I., Paunov, V.N., and Pamme, N. On-chip polyelectrolyte coating onto magnetic droplets–towards continuous flow assembly of drug delivery capsules. *Lab on a Chip*, 17(22):3785–3795, 2017.

[2] Banerjee, U., Misra, S., and Mitra, S.K. Liquid–liquid encapsulation of ferrofluid using magnetic field. *Advanced Materials Interfaces*, 9(21):2200288, 2022.

[3] Tarn, M.D., Fakhrullin, R.F., Paunov, V.N., and Pamme, N. Microfluidic device for the rapid coating of magnetic cells with polyelectrolytes. *Materials Letters*, 95: 182–185, 2013.

[4] Navi, M., Kieda, J., and Tsai, S.S.H. Magnetic polyelectrolyte microcapsules via water-in-water droplet microfluidics. *Lab on a Chip*, 20(16):2851–2860, 2020.

[5] Yang, M., Wu, X., Li, H., Cui, G., Bai, Z., Wang, L., Kraft, M., Liu, G., and Wen, L. A novel rare cell sorting microfluidic chip based on magnetic nanoparticle labels. *Journal of Micromechanics and Microengineering*, 31(3):034003, 2021.

[6] Qiao, R., Fu, C., Forgham, H., Javed, I., Huang, X., Zhu, J., Whittaker, A.K., and Davis, T.P. Magnetic iron oxide nanoparticles for brain imaging and drug delivery. *Advanced Drug Delivery Reviews*, 197:114822, 2023.

[7] Dasgupta, S., Auth, T., and Gompper, G. Nano-and microparticles at fluid and biological interfaces. *Journal of Physics: Condensed Matter*, 29(37):373003, 2017.

[8] Betancourt, S.N.M., Uranga, J.G., Juarez, A.V., Cámara, C.I., López, G.P., and Riva, J.S. Effect of bare and polymeric-modified magnetic nanoparticles on the drug ion transfer across liquid/liquid interfaces. *Journal of Electroanalytical Chemistry*, 919:116502, 2022.

[9] Betancourt, S.N.M., Cámara, C.I., Juarez, A.V., and Riva, J.S. Magnetically controlled insertion of magnetic nanoparticles into membrane model. *Biochimica et Biophysica Acta (BBA)-Biomembranes*, 1866(3):184293, 2024.

[10] Hedayatnasab, Z., Abnisa, F., and Daud, W.M.A.W. Review on magnetic nanoparticles for magnetic nanofluid hyperthermia application. *Materials & Design*, 123: 174–196, 2017.

[11] Schwaminger, S.P., Busse, M., Amiel, T., Srinivasan, S., Turrina, C., Ebel, F., and Straub, M. Magnetic kidney stone removal. In *Current Directions in Biomedical Engineering*, volume 10, pages 17–20. De Gruyter, 2024.

[12] Sinha, A., Mollah, A.K., Hardt, S., and Ganguly, R. Particle dynamics and separation at liquid–liquid interfaces. *Soft Matter*, 9(22):5438–5447, 2013.

[13] Ruiz-Martín, D., Rivero-Rodriguez, J., and Sánchez-Sanz, M. Solid particles moving parallel to a deformable liquid–liquid interface in a micro-channel: migration forces. *Journal of Fluid Mechanics*, 948:A44, 2022.

[14] Driscoll, C.F., Morris, R.M., Senyei, A.E., Widder, K.J., and Heller, G.S. Magnetic targeting of microspheres in blood flow. *Microvascular Research*, 27(3):353–369, 1984.

[15] Grief, A.D. and Richardson, G. Mathematical modelling of magnetically targeted drug delivery. *Journal of Magnetism and Magnetic Materials*, 293(1):455–463, 2005.

[16] Friedman, G. and Yellen, B. Magnetic separation, manipulation and assembly of solid phase in fluids. *Current Opinion in Colloid & Interface Science*, 10(3):158–166, 2005.

[17] Tsai, S.S.H., Griffiths, I.M., Li, Z., Kim, P., and Stone, H.A. Interfacial deflection and jetting of a paramagnetic particle-laden fluid: theory and experiment. *Soft Matter*, 9(35):8600–8608, 2013.

[18] Purcell, E. *Electricity and Magnetism*. Cambridge University Press, 2011. ISBN 9781139503556. URL `https://books.google.co.uk/books?id=Z3bkNh6h4WEC`.

[19] Cullity, B.D. and Graham, C.D. *Introduction to Magnetic Materials*. Wiley, 2009. ISBN 9780470386316. URL `https://books.google.co.uk/books?id=ixAe4qIGEmwC`.

[20] Suwa, M., Tsukahara, S., and Watarai, H. Applications of magnetic and electromagnetic forces in micro-analytical systems. *Lab on a Chip*, 23(5):1097–1127, 2023.

[21] Cappelli, S., Xie, Q., Harting, J., de Jong, A., and Prins, M. Dynamic wetting: status and prospective of single particle based experiments and simulations. *New biotechnology*, 32(5):420–432, 2015.

[22] Livitz, D., Dhatt-Gauthier, K., and Bishop, K.J. Magneto-capillary particle dynamics at curved interfaces: inference and criticism of dynamical models. *Soft Matter*, 19(46):9017–9026, 2023.

[23] Martínez-Pedrero, F. Static and dynamic behavior of magnetic particles at fluid interfaces. *Advances in Colloid and Interface Science*, 284:102233, 2020.

[24] Kichatov, B., Korshunov, A., Sudakov, V., Gubernov, V., Golubkov, A., Kolobov, A., Kiverin, A., and Chikishev, L. Motion of magnetic motors across liquid–liquid interface. *Journal of Colloid and Interface Science*, 652:1456–1466, 2023.

[25] Ramos Docampo, M.A. Magnetic motors in interphases: Motion control and integration in soft robots. *Biointerphases*, 19(4), 2024.

[26] Banerjee, U., Raj, A., and Sen, A. Dynamics of aqueous ferrofluid droplets at coflowing liquid–liquid interface under a non-uniform magnetic field. *Applied Physics Letters*, 113(14), 2018.

[27] de Hemptinne, A., Gelin, P., Ziemecka, I., and De Malsche, W. Microfluidic device for multilayer coating of magnetic microparticles. *Powder Technology*, 416:118223, 2023.

[28] Gunjan, M.R., Banerjee, U., Misra, S., and Mitra, S.K. Manipulation of ferrofluid-wrapped drops: Translation, coalescence, and release. *Advanced Materials Interfaces*, page 2300144, 2023.

[29] Deng, J., Molaei, M., Chisholm, N.G., Yao, T., Read, A., and Stebe, K.J. Active colloids on fluid interfaces. *Current Opinion in Colloid & Interface Science*, 61: 101629, 2022.